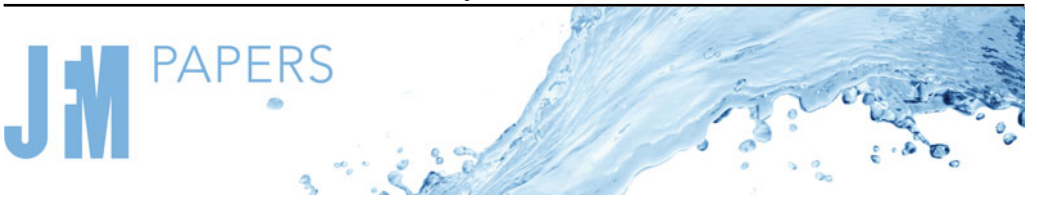
J. Fluid Mech. (2025), *vol.* 1019, A55, doi:10.1017/jfm.2025.10604



Efficiency of turbulence

Adrien Lopez[1], **Amaury Barral**[1], **Guillaume Costa**[1], **Quentin Pikeroen**[1], **Vishwanath Shukla**[2] **and Berengere Dubrulle**[1]

[1]Université Paris-Saclay, CEA, CNRS, SPEC, 91191 Gif-sur-Yvette, France

[2]Department of Physics, Indian Institute of Technology Kharagpur, Kharagpur, India

Corresponding author: Berengere Dubrulle, berengere.dubrulle@cea.fr

(Received 3 March 2025; revised 1 August 2025; accepted 4 August 2025)

We consider the efficiency of turbulence, a dimensionless parameter that characterises the fraction of the input energy stored in a turbulent flow field. We first show that the inverse of the efficiency provides an upper bound for the dimensionless energy injection in a turbulent flow. We analyse the efficiency of turbulence for different flows using numerical and experimental data. Our analysis suggests that efficiency is bounded from above, and, in some cases, saturates following a power law reminiscent of phase transitions and bifurcations. We show that for the von Kármán flow the efficiency saturation is insensitive to the details of the forcing impellers. In the case of Rayleigh–Bénard convection, we show that within the Grossmann and Lohse model, the efficiency saturates in the inviscid limit, while the dimensionless kinetic energy injection/dissipation goes to zero. In the case of pipe flow, we show that saturation of the efficiency cannot be excluded, but would be incompatible with the Prandtl law of the drag friction coefficient. Furthermore, if the power-law behaviour holds for the efficiency saturation, it can explain the kinetic energy and the energy dissipation defect laws proposed for shear flows. Efficiency saturation is an interesting empirical property of turbulence that may help in evaluating the 'closeness' of experimental and numerical data to the true turbulent regime, wherein the kinetic energy saturates to its inviscid limit.

Key words: turbulence theory, turbulence simulation, pipe flow

1. Introduction

Joule's experiment of 1845 showed that when water in a bucket is mechanically stirred, the temperature of the water rises. The experiment illustrates the conversion of mechanical energy into thermal energy in fluids in agreement with the first law of thermodynamics. Richardson cascade phenomenology suggests that this energy conversion is achieved via

© The Author(s), 2025. Published by Cambridge University Press. This is an Open Access article, distributed under the terms of the Creative Commons Attribution licence (https://creativecommons.org/licenses/by/4.0/), which permits unrestricted re-use, distribution and reproduction, provided the original article is properly cited.

https://doi.org/10.1017/jfm.2025.10604 Published online by Cambridge University Press

a two-step process: first, the creation of finer and finer energy-transporting structures, also called eddies; then, when the size of the structures is reduced to the Kolmogorov length η, viscosity effectively transforms the mechanical energy into heat. However, in this process, some finite amount of mechanical energy is stored within the fluid through erratic movements of eddies of all sizes.

The efficiency of this storage can be characterised by introducing a dimensionless number $\mathcal{E} = E/E_f$, where E is the stored kinetic energy per unit mass and $E_f = F_0 L_f$ is the measure of the mechanical energy injected per unit mass due to an applied force of magnitude F_0 acting at length scale L_f. Despite its obvious interpretation, this number is seldom used to describe characteristics of turbulence; instead, we often use the Reynolds number $Re = L_f\sqrt{2E}/\nu$ or the Grashof number $Gr = F_0 L_f^3/\nu$, where ν is the fluid viscosity. This allows us to express the efficiency number as $\mathcal{E} = Re^2/2Gr$, or its inverse, the inefficiency $1/\mathcal{E}$ (Eyink & Peng 2024). However, the independence of $\mathcal{E}$ with respect to the viscosity makes it suitable for exploring the asymptotic regimes of turbulence, wherein the viscosity no longer plays a role. In this paper, we show an application of this idea to the problem of intensity of turbulence for injection and dissipation of energy within a flow and its connection to the empirical defect laws that have been recently proposed for turbulent flows near a wall in Chen & Sreenivasan (2021).

2. Efficiency of turbulence

2.1. *Definitions*

We consider the forced incompressible Navier–Stokes equations (INSEs) given by

$$\partial_t \boldsymbol{u} + (\boldsymbol{u}\cdot\boldsymbol{\nabla})\boldsymbol{u} = -\boldsymbol{\nabla} p + \nu\boldsymbol{\Delta}\boldsymbol{u} + \boldsymbol{f}, \tag{2.1}$$

$$\boldsymbol{\nabla}\cdot\boldsymbol{u} = 0, \tag{2.2}$$

where $\boldsymbol{u}$ is the velocity field, p is the pressure, $\boldsymbol{f}$ is the external force, ν is the viscosity and the constant density is set to $\rho = 1$. We define the total kinetic energy $E = \langle \boldsymbol{u}\cdot\boldsymbol{u}\rangle/2$ and the forcing amplitude $F_0 = \langle \boldsymbol{f}\cdot\boldsymbol{f}\rangle^{1/2}$, where $\langle\cdot\rangle$ denotes the spatial average. We further introduce L_f, a characteristic forcing length scale defined by

$$\frac{(2\pi)^2}{L_f^2} = \frac{1}{3}\frac{\langle \boldsymbol{\nabla}\boldsymbol{f}\cdot\boldsymbol{\nabla}\boldsymbol{f}\rangle}{\langle \boldsymbol{f}\cdot\boldsymbol{f}\rangle}. \tag{2.3}$$

We can then non-dimensionalise the Navier–Stokes equation (2.1) using $\sqrt{2E}$ as unit of velocity and L_f as unit of length:

$$\partial_t \tilde{\boldsymbol{u}} + (\tilde{\boldsymbol{u}}\cdot\boldsymbol{\nabla})\tilde{\boldsymbol{u}} = -\boldsymbol{\nabla}\tilde{p} + \frac{1}{Re}\boldsymbol{\Delta}\tilde{\boldsymbol{u}} + \frac{1}{2\mathcal{E}}\tilde{\boldsymbol{f}}, \tag{2.4}$$

$$\boldsymbol{\nabla}\cdot\tilde{\boldsymbol{u}} = 0, \tag{2.5}$$

where $\tilde{\boldsymbol{u}}$ and $\tilde{\boldsymbol{f}}$ are variables of unit average norm and

$$Re = \frac{\sqrt{2E}L_f}{\nu},$$

$$\mathcal{E} = \frac{\langle \boldsymbol{u}\cdot\boldsymbol{u}\rangle}{2L_f\langle \boldsymbol{f}\cdot\boldsymbol{f}\rangle^{1/2}} \tag{2.6}$$

are the Reynolds number and the efficiency. This non-dimensionalisation illustrates that the parameter space depends on both Re and $\mathcal{E}$. In most applications, one fixes F_0, L_f and ν and measures $\langle E\rangle$. This amounts to fixing the Grashof number $Gr = Re^2/\mathcal{E}$ as the

https://doi.org/10.1017/jfm.2025.10604 Published online by Cambridge University Press

external control parameter, and using Re and $\mathcal{E}$ as diagnostic parameters. However, one could also fix either Re or $\mathcal{E}$ as the control parameter, and measure the other one as a diagnostic parameter (see below).

2.2. *Energy injection*

The energy injected per unit mass ϵ is given by

$$\epsilon = \langle \boldsymbol{f} \cdot \boldsymbol{u} \rangle. \tag{2.7}$$

In stationary turbulence, and in the absence of any singularities, energy injection equals the energy dissipation on average. In many applications, we are interested in knowing the amount of work per unit volume ϵ that must be performed to maintain a fluid of viscosity ν, stirred by an external force of magnitude F_0, in a stationary state characterised by a mean kinetic energy per unit mass $\langle E \rangle$. This will require us to study ϵ as function of ν and $\langle E \rangle$, or, in dimensionless form, $D_\epsilon = (|\epsilon| L_f)/(\sqrt{2}E^{3/2})$ as a function of Re. In this study, we also focus on another problem, namely the amount of viscosity ν required to sustain a given mean mechanical energy per unit mass $\langle E \rangle$ in a fluid, when acted upon by a force of magnitude F_0. In dimensionless form, this corresponds to studying $1/Re$ as a function of $\mathcal{E}$.

The previous discussion holds for incompressible, homogeneous isotropic turbulence in a statistically stationary state. Wall-bounded turbulence like pipe flow adds additional boundary terms to the energy balance, but can still be approached using the efficiency prism, as we show below. Similarly, convection adds new energy source terms, but we show that it can benefit from the efficiency consideration. In what follows, we focus on incompressible flow, as the formalism would need some revisions for compressible flow.

The problems of finding $D_\epsilon(Re)$ and $1/Re(\mathcal{E})$ are clearly related. In fact, obvious inequalities connect the two problems.

2.3. *Exact bounds*

There are a number of exact bounds that link D_ϵ, the dimensionless energy injection, and $\mathcal{E}$, the efficiency. The Cauchy–Schwartz inequality allows us to write

$$D_\epsilon \leqslant \frac{1}{\mathcal{E}}, \tag{2.8}$$

wherein the equality is achieved when $\boldsymbol{f}$ is parallel to $\boldsymbol{u}$. This mathematical inequality is valid independently of any dynamical considerations. If we further focus on the stationary state, we can use energy balance on the Navier–Stokes equations to infer that ϵ is equal to the viscous energy dissipation $\epsilon_\nu = \nu \langle \|\boldsymbol{\nabla} \times u\|^2 \rangle$, which is positive. Therefore, $\epsilon = \epsilon_\nu > 0$ so the absolute value is unnecessary in this specific case.

The properties of the INSEs enable us to derive the following two other inequalities valid in a stationary state (see Doering & Foias 2002):

$$\epsilon \leqslant c_1 \nu \frac{E}{L_f^2} + c_2 \frac{E^{3/2}}{L_f}, \tag{2.9}$$

$$\mathcal{E} \geqslant c_3 + c_4 Gr^{-1} \left(1 - \sqrt{1 + 2c_3 Gr/c_4}\right), \tag{2.10}$$

where c_i are non-universal constants that depend on the properties of the external forcing mechanism. Note that Doering & Foias (2002) claim that the results hold true for the energy dissipation, but the proof is really given for the energy injection ϵ, which is equal to the energy dissipation only for non-dissipative stationary weak solutions. Also, the second inequality comes from equation (50) of Doering & Foias (2002), before the substitution

https://doi.org/10.1017/jfm.2025.10604 Published online by Cambridge University Press

Name	Symbol	Formula
Reynolds number	Re	$L_f\sqrt{2E}/\nu$
Dimensionless energy injection/dissipation	D_ϵ	$\epsilon L_f/E^{3/2}$
Efficiency	$\mathcal{E}$	EL_f/F_0

Table 1. Various dimensionless quantities used in this paper as a function of the fluid kinetic energy E, viscosity ν, forcing intensity F_0 and scale L_f.

for the Taylor microscale is done. We remark that the limit $Gr \to \infty$ implies that the efficiency is bounded from below, $\mathcal{E} \geqslant c_3$.

The above observations show that the efficiency cannot vanish in the limit $Gr \to \infty$. If it can diverge in the same limit, the upper bound (2.8) shows that it would correspond to a solution in which the dimensionless energy injection tends to 0, while at the same time being able to store an infinite energy at finite forcing, a somewhat physically puzzling result. If it were to tend to a finite value in the limit $Gr \to \infty$, it would correspond to a new interesting law of turbulence. Indeed, (2.8) indicates that we can have an efficiency saturating in the inviscid limit, while at the same time an energy injection tending to 0. This shows that the saturation of efficiency and of energy injection/dissipation are different problems.

Below we discuss several examples that clearly illustrate these different points, for different types of turbulence. We summarise various dimensionless quantities of interest in table 1.

3. Empirical tests of the efficiency saturation

3.1. *From numerical data*

Numerical data are obtained from numerical simulations of (2.1) for two types of viscosities: (i) for time-independent (fixed) viscosity, corresponding to the classical Navier–Stokes (NS) situation, in which the total kinetic energy E fluctuates dynamically in time; (ii) for time-independent total kinetic energy E, which is achieved by monitoring in time the viscosity according to

$$\nu = \frac{\langle u \cdot f \rangle}{\langle \|\boldsymbol{\nabla} \times u\|^2 \rangle}. \tag{3.1}$$

This case is referred to as the reversible Navier–Stokes (RNS) case, because it can be shown that such prescription restores the time-reversibility of (2.1), which is broken by the addition of a viscosity. The equivalence of the two models on global quantities was originally conjectured by Gallavotti (1996), and checked in Shukla *et al.* (2019) and Costa, Barral & Dubrulle (2023), so the two types of data can be used on the same footing. Numerically, simulations of RNS equations are more challenging, so that available resolutions are lower. However, the efficiency saturation is easier to control via RNS than NS: instead of varying the Reynolds number to report the corresponding variations of energy, it is now possible to impose the energy and obtain the corresponding Reynolds number. It therefore allows for cleaner saturation laws at more modest Reynolds number.

3.1.1. *The NS equations projected on a logarithmic lattice*

We first illustrate the above idea using a simplified model of fluid turbulence obtained by projecting the NS equations onto a Fourier lattice with exponentially spaced modes.

https://doi.org/10.1017/jfm.2025.10604 Published online by Cambridge University Press

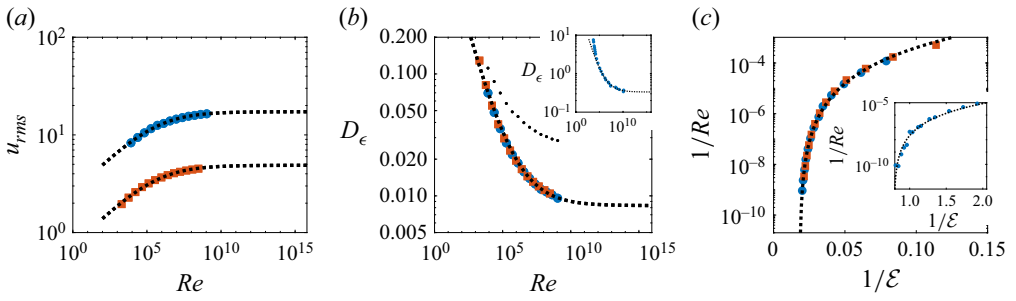


Figure 1. Scaling laws of turbulence on log-lattice. (*a*) The RMS velocity as a function of Reynolds number. The data are the symbols. The black dashed line is the fit, assuming a power law for the efficiency, with corresponding $R^2 = 0.9987$. (*b*) Dimensionless dissipation as a function of Reynolds number. The data are the symbols. The black dotted line is the theoretical bound $\sqrt{2}/\mathcal{E}$, and the dashed line is the fit $\epsilon_*/\mathcal{E}^{3/2}$, with corresponding $R^2 = 0.9960$. (*c*) Viscosity (inverse Reynolds number) versus inefficiency (inverse efficiency). A second-order phase transition is observed where viscosity vanishes at finite inefficiency (Costa *et al.* 2023). Colour codes the forcing type: orange, constant power; blue, constant forcing amplitude. The black dashed line is a fit, assuming a power law for the efficiency, with $R^2 = 0.9576$. These log-lattice simulations were done with $\lambda = 2$ and the insets with $\lambda = \phi$.

The Fourier modes are given by $k_n = k_0\lambda^n$, where λ is the log-lattice parameter (chosen to be 2 or $\phi = 1 + \sqrt{5}/2$ in our simulations). This projection restricts the number of possible interactions between modes, but obeys the symmetries and the global conservation laws associated with the fluid flow. For detailed theoretical and numerical discussions we refer the reader to Campolina & Mailybaev (2018, 2021), Campolina (2019) and Pikeroen *et al.* (2024).

In figure 1 we show our results obtained from the log-lattice simulations of (2.1) in three dimensions with a forcing $\boldsymbol{f}$ of amplitude F_0 around a wavenumber $k_f = 2\pi/L_f$ for different values of viscosity. In these simulations, we use a dyadic spacing $\lambda = 2$ and a golden number spacing $\lambda = \phi = 1.618$ with a maximal wavenumber k_{max} up to 3×10^6. We accumulate various statistics of Fourier modes once a statistically stationary state has been achieved. In particular, we define the kinetic energy E and the energy injection as

$$E = \frac{1}{2}\sum_k \overline{u(k,t)u(-k,t)} \quad \text{and} \quad \epsilon = \sum_k \overline{u(k,t)f(-k,t) + u(-k,t)f(k,t)}, \tag{3.2}$$

respectively, where the overline denotes a time average. Note that in a stationary state, ϵ also represents the mean energy dissipation and $u_{rms} = \sqrt{2E}$ represents the root-mean-square (RMS) velocity, since the mean flow is zero. We use these quantities to define the Reynolds number $Re = L_f\sqrt{2E}/\nu$, the dimensionless energy injection/dissipation $D_\epsilon = \epsilon L_f/E^{3/2}$ and the efficiency $\mathcal{E} = EL_f/F_0$ (also see table 1).

Figure 1(*a*) shows that despite attaining fairly high Re in our log-lattice simulations, the RMS velocity is yet to reach a saturation, believed to be a hallmark of fully developed turbulence. Similarly, the dimensionless energy dissipation D_ϵ continues to decrease as Re is increased; however, near the largest Re the decay rate has decreased, but D_ϵ is still far from saturating. Note that the saturation of the energy dissipation to a constant value is a hallmark of the dissipation anomaly. We also observe that for the Re considered here, the bound $D_\epsilon \leqslant \sqrt{2}/\mathcal{E}$ given by (2.8) is always satisfied. In figure 1(*c*) we show the behaviour of $1/Re$ versus $1/\mathcal{E}$ for the dyadic lattice. The saturation curve can be very well fitted by

https://doi.org/10.1017/jfm.2025.10604 Published online by Cambridge University Press

an implicit power law as

$$\frac{1}{Re} = A\left(\mathcal{E}^{-1} - {\mathcal{E}_*}^{-1}\right)^{\gamma}, \tag{3.3}$$

with $A = 10^{-4.86}$, $\mathcal{E}_* = 55$ and $\gamma = 3.45$. The efficiency saturation in turn provides a dissipation anomaly, following the law with leading-order asymptotic expansion (see figure 1*b*):

$$D_\epsilon = \frac{\epsilon_*}{\mathcal{E}^{3/2}} = \frac{\epsilon_*}{\mathcal{E}_*^{3/2}}\left(1 + \frac{3}{2}\frac{\mathcal{E}_*}{(ARe)^{1/\gamma}}\right) + o(Re^{-1/\gamma}). \tag{3.4}$$

Power laws of such type are found in phase transition or in bifurcation, and it is not accidental that we find it here. It was indeed shown in Costa *et al.* (2023) that solutions of the RNS equations projected on log-lattices display a bifurcation at the value $\mathcal{E}_*$: above $\mathcal{E}_*$, only self-similar blow-up solutions of Euler equations are observed. Below $\mathcal{E}_*$, dissipative irreversible solutions of the NS equations are observed. Such bifurcation can be observed in the behaviour or the enstrophy, that diverges above $\mathcal{E}_*$, while staying finite below $\mathcal{E}_*$. Considering the equivalence of NS and RNS, we thus conclude that the power law we find in our NS case is just the counterpart of the power law observed in RNS. Note, however, that in the NS case, we do not have a phase transition, since we observe only one 'phase', the dissipative irreversible solutions of NS equations. The only caveat is that the warm phase where thermalisation occurs is also accessible for NS by using an under-resolved Galerkin truncated direct numerical simulation (DNS).

The case $\lambda = \phi$ can also be well described by a power law. Specifically, we obtain a good fit for the efficiency using the following set of coefficients: $A = 10^{-0.85}$, $\mathcal{E}_* = 1.27$ and $\gamma = 3.45$ (see the inset of figure 1*c*). This may only be two cases, but the different forcing and lattice spacing suggest that the scaling exponents are universal.

Now, once we obtain the fit, we can invert (3.3) to get u_{rms} as a function of Re. We show this in figure 1(*a*) using black dashed lines. The extrapolation to large Reynolds numbers indicates that the saturation is not observed until $Re \sim 10^{12}$, which is considerably beyond our computational capacity. Similarly, we can use this law to fit the variation of the energy dissipation with Re in figure 1(*b*) and extrapolate predictions for small viscosities. We find that a good fit to the data is given by $D_\epsilon = \epsilon_*/\mathcal{E}^{3/2}$, where $\mathcal{E}(Re)$ is obtained by inverting (3.3) with constant $\epsilon_* = 53$ ($\epsilon_* = 8$) for $\lambda = 2$ ($\lambda = \phi$). The extrapolated black dashed curve suggests that the dimensionless energy dissipation becomes constant in the limit of vanishing viscosity, which is consistent with the existence of dissipation anomaly (the so-called zeroth law of turbulence).

3.1.2. *Direct numerical simulation of RNS equations*

We now repeat the analysis for the homogeneous isotropic turbulence obtained using the DNS of the RNS equations over a triply period domain of size $(2\pi)^3$. For more details we refer the reader to Shukla *et al.* (2019). In RNS, the imposition of a global constraint of the conservation of a quadratic quantity, for example the total energy, allows for the viscosity $\nu(t)$ to fluctuate in time; however, its statistical properties are equivalent to those obtained using the standard INSE (2.1). We use two different codes: S1, a classical pseudo-spectral code with 64^3 and 128^3 collocation points, and S2, a pseudo-spectral code with Taylor–Green symmetries that allows us to perform DNS with 512^3 and 1024^3 collocation points. Note that the Reynolds numbers reached here are considerably smaller than those of log-lattice simulations.

https://doi.org/10.1017/jfm.2025.10604 Published online by Cambridge University Press

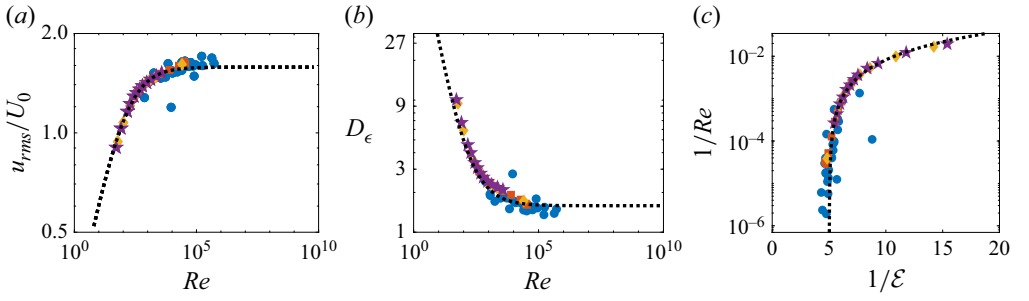


Figure 2. Scaling laws of turbulence in numerical homogeneous isotropic turbulence. (*a*) The RMS velocity as a function of Reynolds number. To account for different forcing type, we have divided the RMS velocity by $U_0 = \sqrt{F_0 L_f}$. The data are the symbols. The black dashed line is the fit, assuming a power law for the efficiency, with $R^2 = 0.9844$. (*b*) Dimensionless dissipation as a function of Reynolds number. The data are the symbols. The dashed line is the fit $2.5/\mathcal{E}^{3/2}$, with $R^2 = 0.8733$. (*c*) Viscosity (inverse Reynolds number) versus inefficiency (inverse efficiency). Red and yellow symbols: S1 at resolution 64^3 and 128^3; magenta and blue symbols: S2 at resolution 512^3 and 1024^3. The black dashed line is a fit, assuming a power law for the efficiency, with $R^2 = 0.9706$. Here *Re* is not explored as far as in log-lattice simulations, but the phase transition/bifurcation begins at smaller *Re*, with a larger inefficiency compared with log-lattice simulations.

Figures 2(*a*) and 2(*b*) show that despite the comparatively smaller Reynolds numbers, both u_{rms}/U_0 and the dimensionless dissipation, respectively, begin to saturate for $Re \simeq 10^4$. Similarly $1/Re$ starts to show saturation starting at $\mathcal{E}_* \sim 0.2$ (see figure 2*c*). A fit of the form (3.3) is obeyed with the exponent $\gamma = 1.4$ and the prefactor $A = 10^{-0.2}$. Inversion of this power law allows us to obtain a parameter-free fit of the kinetic energy in figure 2(*a*) and a one-parameter fit of the energy dissipation $2.5\mathcal{E}^{-3/2}$. In summary, the DNS results are very similar to the case of the flows projected on log-lattices, but belong to a different 'universality class' (laws have the same shape but different constants). Given the equivalence between RNS and NS, we can trace this difference to the number of allowed triadic interactions in Fourier space.

3.1.3. *Comment on the dissipation scaling*

Through the efficiency lens, we are able to connect energy dissipation and the Reynolds number by inverting the power law, resulting in (3.4). It is instructive to compare the asymptotic behaviour of the dissipation anomaly with other simple models. A qualitatively similar formula can be obtained by a mean field approach:

$$D_\epsilon = D_{\epsilon,\infty}\left(\sqrt{1+\frac{3b^3}{8}\frac{1}{Re^2}}+\sqrt{\frac{3b^3}{8}\frac{1}{Re}}\right) = D_{\epsilon,\infty}\left(1+\sqrt{\frac{3b^3}{8}\frac{1}{Re}}\right)+o(Re^{-1}), \quad (3.5)$$

where b is the Kolmogorov constant for the two-point structure constant. A full derivation can be found in Lohse (1994). This theoretical approach has the benefit of predicting that $\gamma = 1$. This is not specific to the chosen closure model of the article akin to a turbulent viscosity:

$$\nu_t = \frac{D^2}{b^3\epsilon}, \quad (3.6)$$

where D is the two-point structure function. Any closure at the level of the two-point correlation function will necessarily give $\gamma = 1$. This follows from the Kármán–Howarth equation itself. In the inviscid case, the third-order structure function expressed in terms

https://doi.org/10.1017/jfm.2025.10604 Published online by Cambridge University Press

of D, ϵ but independent of ν (given by the choice of closure) balances the dissipation term, with a finite dissipation rate solution. The viscous term is proportional to ν, and will therefore generically give a $O(\nu) = O(Re^{-1})$ correction to the asymptotic dissipation rate. In statistical mechanics, the analogue would be the Landau theory whose structural limitations only allow it to predict mean-field critical exponents. To reproduce the numerical data, where $\gamma = 3.4$ for log-lattice or $\gamma = 1.4$ for DNS, the full hierarchy of structure functions seems to be necessary, requiring at least some analogue of the renormalisation group to recover the anomalous scaling.

3.2. *From experimental data*

So far, all the results were obtained in well-controlled situations, where all the quantities are known exactly. We now turn to the case of experimental flows, to show how the efficiency can be computed from classical global diagnostics of the flow and possible incomplete data.

3.2.1. *Von Kármán flows*

First, we consider the von Kármán flow generated between two counter- or co-rotating impellers in a cylindrical tank. The experimental set-up has impellers of radius R_d in a tank of radius R filled with a fluid of density ρ and viscosity ν. The distance between the two impellers is $H = 1.8R$. The fluid is forced and maintained in a turbulent state at a high Reynolds number by means of the two independently rotating impellers at the same constant frequency F, located at the top and the bottom of the cylindrical tank. Flows with different Reynolds numbers are achieved by using different fluids: pure glycerol, mixture of glycerol and water, and water at $T = 20\,^{\circ}\mathrm{C}$. In all the cases, the temperature is kept constant through a thermal regulation, to avoid drifts of viscosity during operation. The mean kinetic energy of the flow can be computed on a meridian plane, including the rotation plane, with the help of the stereoscopic particle image velocimetry technique, which allows for the reconstruction of the three components of the velocity within this plane. For further technical details about these measurements, we refer the reader to Monchaux (2007), Debue (2019) and Cortet *et al.* (2009, 2010).

The axisymmetry of the flow ensures that the planar estimate is equal to the volume average of the kinetic energy. Moreover, inserting two torque meters, before and below the top and bottom impellers, respectively, allows for the measurement of the torque $\Gamma(t)$ applied by the turbulent flow on the impeller; this provides an estimate of the amplitude of the forcing per unit mass required to maintain the flow in a stationary state. The energy dissipation rate is measured using the mean injection rate, obtained by computing the mean work done by the torque $W = \overline{\Gamma(t) F}$, where the overline denotes a time average. The choice of the unit of length $L = R$ and the unit of velocity $U = 2\pi R F$ allows us to combine the parameters summarised in table 2 into the mean torque K_p, the kinetic energy E and the global Reynolds number Re_F in dimensionless form as follows:

$$K_p = \frac{\overline{\Gamma}}{\rho \pi R^5 (2\pi F)^2}, \quad E = \frac{\langle \boldsymbol{u} \cdot \boldsymbol{u} \rangle^{1/2}}{2(2\pi R F)^2} \quad \text{and} \quad Re_F = \frac{2\pi R^2 F}{\nu}, \tag{3.7}$$

respectively, where $\langle \cdot \rangle$ denotes an average over the meridian plane. In that experimental configuration, the mean torque provides two points of information. First, it directly provides the mean force applied to the flow by the propellers, providing an estimate of F_0. Second, it can also provide the energy injection/dissipation ϵ in experimental conditions where the velocities of the upper and lower impellers are maintained constant in time. Indeed, in such a case, the mean power injected at the top and the bottom is computed

https://doi.org/10.1017/jfm.2025.10604 Published online by Cambridge University Press

Name	Symbol	Description/formula
Radius	R_d, R	Impeller, tank radius
Height	H	Distance between impellers ($H/R = 1.8$)
Frequency	F	Common rotation frequency of impellers
Torque	Γ	Measured response of the flow
Dimensionless torque	K_p	$\overline{\Gamma}/\rho\pi R^5(2\pi F)^2$
Dimensionless energy	E	$\langle \boldsymbol{u}\cdot\boldsymbol{u}\rangle^{1/2}/2(2\pi RF)^2$

Table 2. Parameters of the von Kármán experiment.

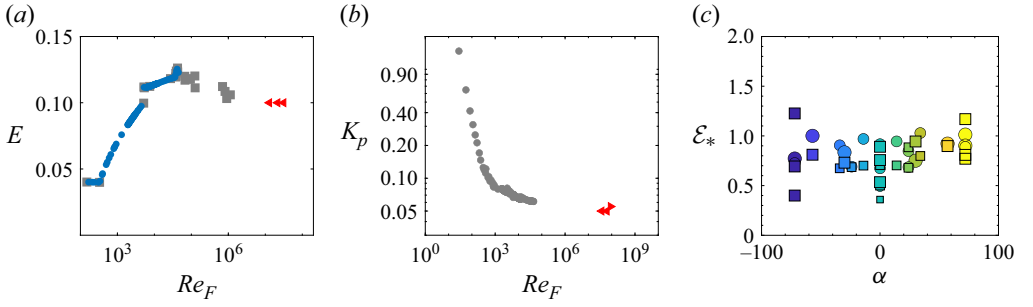


Figure 3. Measurements in von Kármán flow with counter-rotating impellers. (*a*) Kinetic energy E versus global Reynolds number Re_F. Grey symbols correspond to the real data from particle image velocimetry, while the blue symbols interpolate the missing data using a supercritical law $E \sim (Re_F - 3500)^{1/2}$ (Ravelet, Chiffaudel & Daviaud 2008). (*b*) Mean dimensionless torque K_p versus Re_F as measured by Ravelet (2005) (grey circles). The red triangles correspond to points measured in the SHREK experiments (superfluid helium) using eight-bladed impellers with curvature 72°. (*c*) Efficiency of impellers of various radii, fitted with blades of curvature angle α.

as the time average of the torque times the frequency of the impeller. The latter being constant, the power is just the product of the mean torque times the (constant) frequency. We are thus in a situation where the equality in (2.8) is realised, so that the two quantities tend to zero or saturate together.

We analyse the data from the experimental runs, wherein the counter-rotating impellers are fitted with 16 curved blades of angle 72° in the scooping direction, resulting in a symmetric large-scale circulation (Ravelet 2005; Cortet *et al.* 2010); such impellers are referred to as TM60+. In figures 3(*a*), 3(*b*) and 3(*c*) we show plots of E, K_p and $\mathcal{E}_*$, respectively, using the available data. We have sparse data points for the kinetic energy in the Reynolds number range $Re_F \in [10^2, 10^6]$ and a detailed set of measurements of the dimensionless torque K_p for the range $Re_F \in [10^2, 10^5]$. To be able to combine both the measurements, we first interpolate the kinetic energy over the range of Reynolds number for which the detailed measurements of K_p exist. We perform the interpolation using the information that the transition from the laminar to turbulent state is supercritical, with an exponent 2 and critical Reynolds number $Re_* = 3500$ (see Ravelet *et al.* 2008). Following this, we compute all the quantities of interest (in dimensionless units):

$$F_0 = \frac{K_p R^2 L_f}{R_d^2}, \quad u_{rms} = \sqrt{2E} \quad \text{and} \quad R_{rms} = u_{rms} L_f Re_F, \tag{3.8}$$

where L_f is the dimensionless forcing scale. For the rest of this discussion, we take L_f to be unity. We show the results of the analysis similar to the numerical data in figure 4.

https://doi.org/10.1017/jfm.2025.10604 Published online by Cambridge University Press

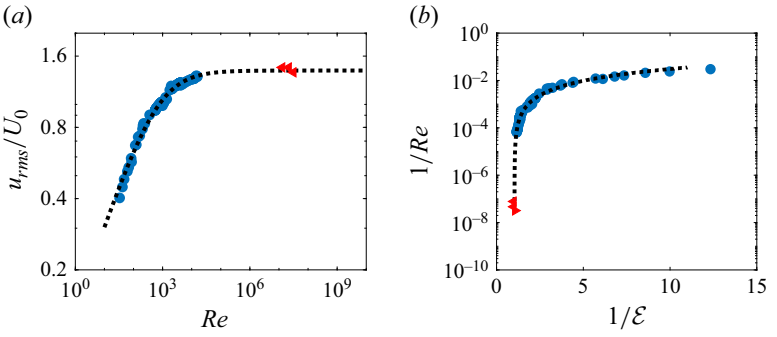


Figure 4. Scaling laws of turbulence in experimental von Kármán flow with counter-rotating TM60+ impellers. (*a*) The RMS velocity as a function of Reynolds number. To account for different forcing amplitude, we have divided the RMS velocity by $U_0 = \sqrt{F_0 L_f}$. The data are the blue symbols. The black dashed line is the fit, assuming a power law for the efficiency, with $R^2 = 0.9915$. (*b*) Viscosity (inverse Reynolds number) versus inefficiency (inverse efficiency). The red triangles correspond to points measured in the SHREK experiments (superfluid helium) using eight-blade impellers (Saint-Michel *et al.* 2014). The black dashed line is the fit, assuming a power law for the efficiency, with $R^2 = 0.9730$.

We do not observe any clear saturation of the quantities u_{rms}/U_0, $D_\epsilon = 1/\mathcal{E}$ and $1/Re$. However, if we assume a power law for the efficiency (3.3), we find a good fit for the parameters $A = 10^{-2.7}$, $\mathcal{E}_* = 0.97$ and $\gamma = 1.4$, which is similar to the homogeneous isotropic turbulence case. Furthermore, we can use this fit to extrapolate the behaviour at higher Reynolds numbers. However, the above discussed experimental runs do not have torque data at further higher Reynolds numbers to check the quality of the extrapolation for the efficiency. Therefore, we use the torque data at very large Reynolds numbers measured in the SHREK facility (Rousset 2014; Saint-Michel 2014; Diribarne 2021). Note that the SHREK set-up has the same geometry as the experimental set-up discussed above, except that the impellers are fitted with 8 blades instead of 16. We show those data in figure 4 using red filled triangles, which lie on the extrapolated behaviour (black dashed line).

We check the dependence of $\mathcal{E}_*$ with respect to the forcing details. To achieve this, we compute the efficiency at $Re_F \sim 10^6$ based on the measurements of K_p and the kinetic energy as reported in Ravelet (2005), wherein these quantities were obtained for impellers of various radii and fitted with blades of different curvature angle α. We find that the data are somewhat scattered, but on an average lie around the value $\mathcal{E}_* \sim 1$, which shows that this value is independent of this geometry. This is rather remarkable, since the value of α has a profound impact on the flow anisotropy, as measured by the ratio between the poloidal and the toroidal energy (Ravelet 2005).

3.2.2. *Pipe flows*

The second experimental flow that we consider is an example of a wall-bounded parallel flow. This is characterised by a mean flow that depends only on one space coordinate; as a consequence, streamlines are parallel. We choose a circular pipe flow and analyse the data available from the experimental works of Swanson *et al.* (2002) and McKeon *et al.* (2004). The flow is driven by a pressure gradient along the axis of the pipe, $\partial_x P$, and results in a mean velocity $\overline{U}$. In smooth pipes, pressure gradients balance the shear stress, so that the force applied to the flow can be measured either through the pressure drop along the pipe or through the friction drag τ_w. For the given fluid density ρ, the viscosity ν and the

https://doi.org/10.1017/jfm.2025.10604 Published online by Cambridge University Press

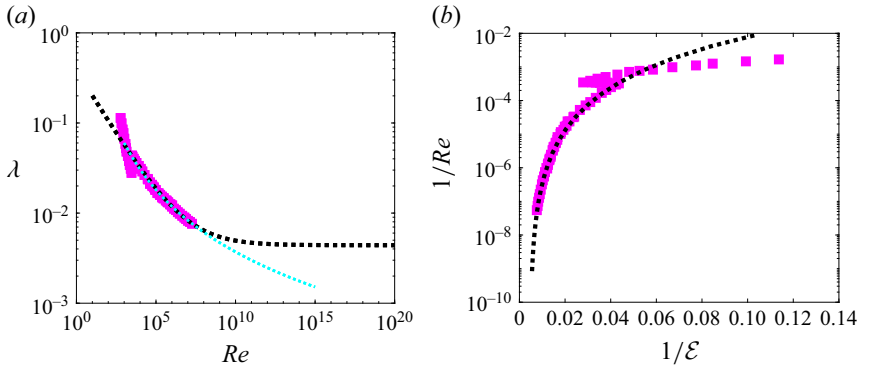


Figure 5. (*a*) Friction factor as a function of Re in pipe flow. The black dotted line is obtained by inverting the power law for efficiency, with $R^2 = 0.9936$. The blue dotted line represents the Prandtl-type formula with $R^2 = 0.9966$. The quality of the fit shows that for these data both laws have similar accuracy. Only experimental data at much higher Reynolds number could discriminate between the two. (*b*) Check of the power law for the efficiency. The dotted line is a fit with a power law of slope 3.5 and $R^2 = 0.9966$.

pipe diameter D, we can build two dimensionless parameters:

$$\lambda = 8\frac{-(\partial_x P)D}{\rho \overline{U}^2} \quad \text{and} \quad Re = \frac{\overline{U}D}{\nu}. \tag{3.9}$$

We show plots of λ versus Re and $1/Re$ versus $\mathcal{E}$ in figures 5(*a*) and 5(*b*), respectively. The force applied to the flow is $F_0 = (1/\rho)\partial_x P$. We further assume that the typical forcing wavenumber is $k_f = 1/D$. To compute the efficiency, we need the kinetic energy E stored in the flow. It can be split into two contributions, following $E = \overline{U}^2/2 + u_{rms}^2/2$. The first term is due to the presence of a mean-flow velocity and the second term is associated with the RMS velocity u_{rms}. However, we have $u_{rms}^2 \ll \overline{U}^2$ because of the presence of a large mean flow. As a consequence we can approximate the kinetic energy as $E = \overline{U}^2/2$. Therefore, with this convention, we have $\lambda \sim 1/\mathcal{E}$. In figure 5(*b*) we show the behaviour of $1/Re$ versus λ (or $\mathcal{E}$), where we observe that it follows the power law (3.3) with an exponent $\alpha = 3.5$. Clearly, this exponent is larger than the one that we obtained for homogeneous isotropic turbulence, which shows a sensibility to anisotropy and inhomogeneity.

When we invert the efficiency power law, we observe a saturation in the behaviour of λ (see figure 5*a*). This is in stark contrast to the Prandtl formula which predicts a decaying behaviour:

$$\lambda = [0.8382\, W(0.6287\, Re)]^{-2} \sim \frac{1}{(0.8382 \ln Re)^2}, \tag{3.10}$$

where W is the Lambert function (Dubrulle 2024). The fit displayed in figure 5(*a*) shows that effect of saturation will only be felt at $Re \sim 10^{12}$, a value way too large for present experimental facilities.

3.2.3. *Taylor–Couette flow*

Taylor–Couette flow is obtained by the co- or counter-rotation of two independent coaxial cylinders, with radii a for the inner cylinder and b for the outer cylinder. Many different experiments have been built to study such flow (Paoletti *et al.* 2012). We use here data from the Twente turbulent TC facility T^3C, kindly provided to us by D. Lohse. The experiment is described in great detail in van Gils *et al.* (2011). It is characterised by cylinders of

https://doi.org/10.1017/jfm.2025.10604 Published online by Cambridge University Press

height $L = 92.7$ cm, and respective radii $a = 20.0$ cm and $b = 27.94$ cm. The maximum inner and outer angular velocities are $\Omega_1/2\pi = 20$ Hz and $\Omega_2/2\pi = \pm 10$ Hz, respectively. The torque is measured over the middle part of the inner cylinder of height $L_{mid} = 53.6$ cm to minimise the influence of the end-plates (similar to Lathrop *et al.* 1992*a*,*b*). This allows for the definition of the dimensionless torque $G = T/\rho\nu^2 L_{mid}$, where T is the torque, ρ the fluid density and ν the kinematic viscosity.

The Taylor–Couette flow is characterised by three essential parameters (Dubrulle *et al.* 2005), namely:

(i) its Reynolds number $Re = (2/1+\eta)|\eta Re_2 - Re_1|$;
(ii) its rotation number $R_\Omega = (1-\eta)(Re_1 + Re_2/\eta Re_2 - Re_1)$;
(iii) its curvature number $R_C = (1-\eta/\eta^{1/2})$;

where $Re_1 = a\Omega_1 d/\nu$ and $Re_2 = b\Omega_2 d/\nu$ are the Reynolds number of the inner and outer cylinder. The above control parameters have been introduced so that their definitions apply to rotating shear flows in general and not only to the Taylor–Couette geometry. It is very easy in this formulation to relate the Taylor–Couette flow to shearing sheet (plane Couette flow with rotation) by simply considering the limit $R_C \to 0$.

Torque measurements provide the force intensity applying to the turbulent flow. Moreover, like in the von Kármán case, it also provides the power through the time average of the product of torque times the frequency. Since frequencies of the inner and outer cylinders are time-independent, we are in a situation where efficiency and energy injection follow the equality in (2.8).

Applying the definition (2.6), we thus obtain that in the case of Taylor–Couette flow, the efficiency and the dimensionless dissipation are given by $\mathcal{E} = (1/D_\epsilon) = (Re^2/G)$. Saturation of the efficiency or of the dimensionless dissipation corresponds to a situation where $G \propto Re^2$. This is called the ultimate regime, in which transport properties no longer depend on the molecular viscosity. Detailed analyses of G as a function of Re and R_Ω have been performed in Dubrulle *et al.* (2005) and Paoletti *et al.* (2012). It was found that for all existing experimental data, it was possible to factorise the torque as $G = f(R_\Omega)G_i$, where f is a function that only depends on R_ω and G_i is the torque computed in a situation where the outer cylinder is at rest. Using this property, we can also factorise the efficiency and the dimensionless energy injection (friction factor) as

$$\mathcal{E} = \frac{1}{D_\epsilon} = \frac{1}{f(R_\Omega)}\frac{Re^2}{G_i}. \tag{3.11}$$

This shows that it is sufficient to consider only the behaviour of Re^2/G_i as a function of Re. This behaviour is reported in figure 6, for a case where only the inner cylinder is rotating. One sees that the friction factor does not saturate, but steadily decays with increasing Re, in the range of Re considered. Even though the range of Reynolds number is not very large, we have tried to see whether the reduced efficiency could be fitted by a power law (3.3) with $A = 10^{-0.73466}$, $\mathcal{E}_* = 44$ and $\gamma = 1.634$. The result is shown in figure 6(*b*). The fit is clearly not as good as for previously considered cases, and it may well be that the efficiency never saturates in this case. Nonetheless, more data would be needed to draw a conclusion.

3.2.4. *Rayleigh–Bénard convection*

The Rayleigh–Bénard setting corresponds to a situation where the fluid is heated from below, and enclosed between two plates, separated by a distance H. The temperature

https://doi.org/10.1017/jfm.2025.10604 Published online by Cambridge University Press

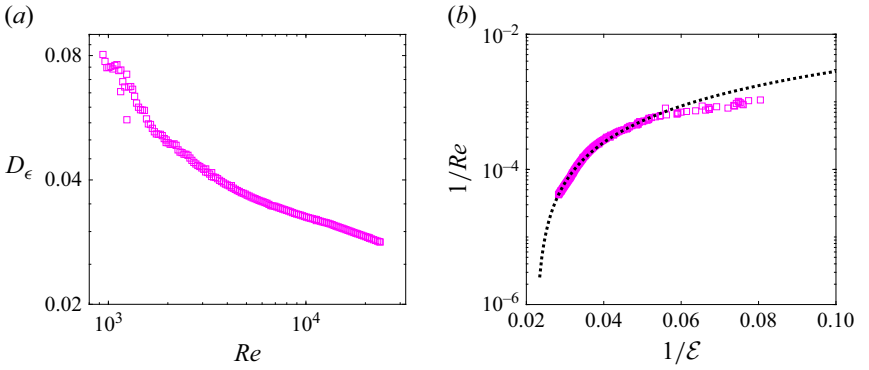


Figure 6. Reduced efficiency and friction factor in Taylor–Couette flow, obtained in a situation where only the inner cylinder is rotating. (*a*) Friction factor as a function of *Re* in Taylor–Couette flow. (*b*) Check of the power law for the efficiency. The dotted line is a power law with exponent 1.634. The fit was performed using only fully turbulent cases, i.e. $Re > 2 \times 10^3$, giving $R^2 = 0.9892$. Data are from the Twente turbulent TC facility T^3 (van Gils *et al.* 2011). Data courtesy of D. Lohse.

difference between the two plates is ΔT. This classical setting has been the topic of many numerical and experimental studies (Roche 2020; Lohse & Shishkina 2024). This is a paradigmatic example of a flow forced by buoyancy. The Rayleigh–Bénard flow is characterised by three dimensionless control parameters, namely:

(i) its Rayleigh number $Ra = (g\beta\Delta T H^3/\kappa\nu)$;
(ii) its Prandtl number $Pr = \nu/\kappa$;
(iii) its aspect ratio $\Gamma = H/L$;

and two dimensionless response parameters:

(i) its Reynolds number $Re = UH/\nu$;
(ii) its Nusselt number (dimensionless heat flux $Nu = JH/\kappa\Delta T$);

where J is the heat flux, $U = \sqrt{2E}$ the typical velocity, g the gravitational acceleration, β the coefficient of thermal expansion, ν the kinematic viscosity, κ the thermal diffusivity and L a typical horizontal scale. In the case of no-slip boundary conditions, the variation of *Nu* and *Re* can been approximated with effective scaling laws, $Nu \sim Pr^\alpha Ra^\gamma$, for which the prefactor and effective exponent depend on the range in $Ra{-}Pr{-}\Gamma$ parameter space. All experiments and numerical simulations reported so far show $\gamma < 1/2$ (Lohse & Shishkina 2024). Through a recent theoretical and experimental effort, the aspect ratio dependence of the heat transfer in a cylindrical volume of various aspect ratios has been elucidated in Ahlers *et al.* (2022), and shown to be amenable to the introduction of a new effective height $H_{eff} = H(\Gamma^2/(1/49 + \Gamma^2)^{1/2}$. An example of data collapse of different aspect ratios and *Pr* is shown in figure 7(*a*) for numerical (Scheel & Schumacher 2017; Stevens *et al.* 2018) and experimental (Chavanne *et al.* 1997; Methivier *et al.* 2022) data at various Γ and *Pr*. There is a mild decay of $Nu/Ra^{1/3}$, followed by a steeper rise at larger Rayleigh numbers, evidencing the transition between $\gamma <\sim 1/3$ and $\gamma > 1/3$ as the Rayleigh number increases. These data have been selected because they offer measurements of both *Nu* and *Re* as a function of Γ, *Pr* and *Ra*, a feature that will be important in the computation of the efficiency (see below). However, they are typical of all data gathered so far. See Ahlers *et al.* (2022) for example of collapse with more data.

https://doi.org/10.1017/jfm.2025.10604 Published online by Cambridge University Press

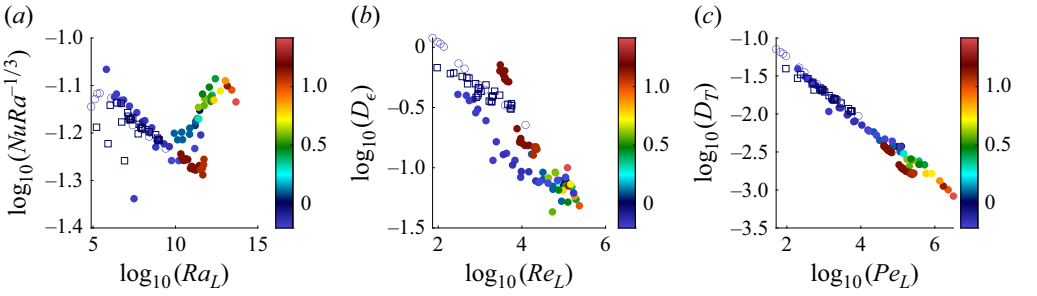


Figure 7. Scaling laws of turbulence in experimental and numerical Rayleigh–Bénard convection. To account for different aspect ratio, we have used everywhere the effective length scale $H_{eff} = H(\Gamma^2/(1/49 + \Gamma^2)^{1/2}$ (Ahlers *et al.* 2022). Filled symbols: experiments by Chavanne *et al.* (1997) and Methivier *et al.* (2022); open squares: numerical data by Stevens *et al.* (2018); open circles: numerical data by Scheel & Schumacher (2017). The data are coloured according to $\log_{10}(Pr)$. (*a*) Rescaled dimensionless heat transfer as a function of Rayleigh number. (*b*) Dimensionless kinetic energy dissipation as a function of Reynolds number. (*c*) Dimensionless thermal energy dissipation as a function of Péclet number. Data courtesy of O. Shishkina.

Theories explaining scaling laws in Rayleigh–Bénard flow are generally based on two exact relations for the kinetic and thermal energy dissipation (Shraiman & Siggia 1990; Lohse & Shishkina 2024):

$$\epsilon_k = \nu^3(Nu - 1)RaPr^{-2}/H^4, \quad \epsilon_t = \kappa(\Delta T)^2 Nu/H^2, \tag{3.12}$$

or in dimensionless form:

$$D_\epsilon = \frac{\epsilon_k H}{U^3} = (Nu - 1)RaPr^{-2}Re^{-3}, \quad D_T = \frac{\epsilon_t H}{(\Delta T)^2 U} = Nu\, Re^{-1}Pr^{-1}. \tag{3.13}$$

Their behaviour as a function of Re or $Pe = RePr$ is shown in figures 7(*b*) and 7(*c*). In both cases, they decay steadily, showing no evidence of saturation. Saturation of both D_ϵ and D_T would correspond to the ultimate regime of convection, in which $Nu \sim RePr \sim (RaPr)^{1/2}$.

The forcing being due to the buoyancy, we have $F_0 = g\beta\Delta T$. Therefore, the efficiency can be simply expressed as a function of the Rayleigh and Reynolds numbers as

$$\mathcal{E} = Re^2 PrRa^{-1}. \tag{3.14}$$

Injecting this into (3.13), we then get $D_\epsilon = (Nu - 1)/(RePr\mathcal{E})$. Because of the exact bound $Nu < RePr$ (Lohse & Shishkina 2024), we see that D_ϵ is indeed bounded by $1/\mathcal{E}$, in accordance with (2.8). This analysis therefore provides an alternative interpretation of the required conditions to get the ultimate, asymptotic regime, as being achieved when both $Nu/(RePr)$ and $\mathcal{E}$ saturate. The verification of such saturation is provided in figure 8. We observe no sign of saturation for either quantity at the Rayleigh numbers investigated.

To investigate the inviscid limit of D_ϵ and $\mathcal{E}$, one can use the extension of the Grossmann and Lohse theory to the ultimate regime (Lohse & Shishkina 2024). This theory identifies four different asymptotic regimes (for $Ra \to \infty$) depending on the scaling of Pr with Ra, namely:

(i) Regime II'_l for $Pr < Ra^{-1}$.
(ii) Regime IV'_l for $Ra^{-1} < Pr < 1$.
(iii) Regime IV'_u for $1 < Pr < Ra^{1/3}$.
(iv) Regime III'_∞ for $Ra^{1/3} < Pr < Ra^{2/3}$.

https://doi.org/10.1017/jfm.2025.10604 Published online by Cambridge University Press

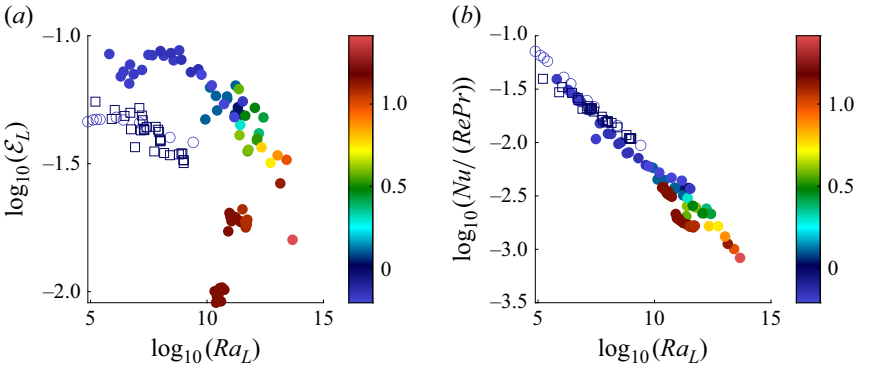


Figure 8. Tests of the ultimate regime in Rayleigh–Bénard convection. (*a*) Efficiency as a function of *Ra*. (*b*) $Nu/RePr$ as a function of *Ra*. Same symbols and colours as in figure 7. Data courtesy of O. Shishkina.

Regime	Nu	Re	D_ϵ	$\mathcal{E}$
II'_l	$Pr^{1/5}Ra^{1/5}$	$Pr^{-3/5}Ra^{2/5}$	$Pr^{0}Ra^{0}$	$Pr^{-1/5}Ra^{-1/5}$
III'_∞	$Pr^{0}Ra^{1/3}$	$Pr^{-1}Ra^{2/3}$	$Pr^{1}Ra^{-2/3}$	$Pr^{-1}Ra^{1/3}$
IV'_l	$Pr^{1/2}(Ra^{1/2}/(\log(Ra))^2)$	$Pr^{-1/2}Ra^{1/2}$	$Pr^{0}(1/(\log(Ra))^2)$	$Pr^{0}Ra^{0}$
IV'_u	$Pr^{-1/2}(Ra^{1/2}/(\log(Ra))^2)$	$Pr^{-1/2}Ra^{1/2}$	$Pr^{-1}(1/(\log(Ra))^2)$	$Pr^{0}Ra^{0}$

Table 3. Variation of the Nusselt number Nu, the Reynolds number Re, the dimensionless dissipation D_ϵ and the efficiency $\mathcal{E}$ as a function of the Rayleigh number Ra and the Prandtl number Pr, in the four asymptotic ultimate regimes identified by Lohse & Shishkina (2024). The last two columns are mere consequences of the definition of D_ϵ and $\mathcal{E}$.

Table 3 summarises the behaviour of the Nusselt number, Reynolds number, dissipation and efficiency in these four regimes. We see that in regimes IV'_l and IV'_u, D_ϵ never achieves saturation at infinite Rayleigh number, at variance with the zeroth law of turbulence, while efficiency saturates to a constant independent of Pr. In contrast, in regime II'_l, dissipation tends to a constant, while efficiency goes to zero. Finally, in regime III'_∞, the dissipation tends to zero and the efficiency to ∞. Rayleigh–Bénard convection therefore provides an example where efficiency and energy dissipation can have different behaviours. Such difference could be used to offer an alternative detection of the ultimate regime.

4. Discussion

A recent work on the probabilistic representation of Kolmogorov's 1949 theory decomposes the turbulence phenomenology into three axioms. The first two are as follows. (A1) The variance of any component of the velocity field remains finite and independent of the viscosity in the long-time and inviscid limit. (A2) The average energy dissipation remains finite in the inviscid limit. Clearly, the 'efficiency saturation' discussed in the present study is connected to (A1), which ensures that $\mathcal{E}$ remains finite in the inviscid limit, so that $1/\mathcal{E}$ cannot tend to zero in the inviscid limit. In the same way, axiom (A2) forbids the energy dissipation from diverging in the inviscid limit. However, none of these axioms 'guarantee' the presence of convergence to a finite non-zero value in the inviscid limit.

https://doi.org/10.1017/jfm.2025.10604 Published online by Cambridge University Press

In view of the above discussion, it is interesting to note that the efficiency saturation is realised for the variety of flows that we consider here. Thus, the efficiency saturation is a robust property of turbulence. Also, saturation is achieved following a power law, which in turn is associated with and motivated by the transitional behaviour of the solutions of the (formally) RNS equations. Our observations also suggest that the coefficients of the power law depend on the flow geometry: the behaviour is steeper (large exponent) for pipe flows when compared with homogeneous turbulence or von Kármán flow. In the latter case, we found that the efficiency is fairly independent of the type of impellers that are used, even when they impart large anisotropies in kinetic energy.

In the case of pipe flow, we show that saturation of the efficiency cannot be excluded but would be incompatible with the Prandtl law of the drag friction coefficient. In the case where the saturation of efficiency follows the power-law behaviour observed for homogeneous isotropic turbulence or von Kármán flow, it can explain the defect laws proposed by Chen & Sreenivasan (2021) for shear flows, for both the peak velocities and the energy dissipation. Indeed, because of the efficiency saturation, the peak velocity variances are necessarily bounded. Thus, by inverting the power law (3.3), we obtain the convergence of the kinetic energy (a proxy of the peak velocity variances) to its limit in accordance with a defect law, $E \sim K - Re^{-\alpha}$, with an exponent $\alpha = 1/3.5 = 0.28$. This is very close to the defect law with $\alpha = 1/4$ proposed by Chen & Sreenivasan (2021). Note that imperfect agreement with the latter law has already been reported in Pirozzoli (2024). They find a smaller exponent $\alpha = 0.18$, but coincidentally, when extrapolating data to high Reynolds number, they obtain a saturation of dissipation rate to a value of 0.28. This saturation can also be explained in the present framework, as the defect law for kinetic energy also applies to the dimensionless energy dissipation D_ϵ, provided ϵ obeys the dissipation anomaly.

In the case of Taylor–Couette flow, the power law could not be firmly established, because more data would be needed.

In the case of Rayleigh–Bénard convection, we show that within the extension of the Grossmann–Lohse model to the ultimate regime (Lohse & Shishkina 2024), the efficiency saturates in the inviscid limit, while the dimensionless kinetic energy injection/dissipation goes to zero. This shows that efficiency and dimensionless energy dissipation are distinct quantities, that can vary independently of each other, provided the dimensionless energy dissipation remains bounded by the inefficiency.

In summary, our study suggests that the efficiency saturation is an interesting empirical property of turbulence that may help in evaluating the 'closeness' of experimental and numerical data to the true turbulent regime, wherein the kinetic energy saturates to its inviscid limit.

Acknowledgements. We thank D. Lohse for providing us with the Taylor–Couette data and O. Shishkina for providing us with the Rayleigh–Bénard data. We thank G. Krstulovic for providing data of reversible Navier–Stokes direct numerical simulations (case S2).

Funding. This work received funding from the Ecole Polytechnique; from ANR BANG, grant agreement no. ANR-22-CE30-0025-01; and from ANR TILT, grant agreement no. ANR-20-CE30-0035.

Declaration of interests. The authors report no conflict of interest.

References

Ahlers, G. *et al.* 2022 Aspect ratio dependence of heat transfer in a cylindrical Rayleigh–Bénard cell. *Phys. Rev. Lett.* **128**, 084501.

Campolina, C.S. 2019 Fluid dynamics on logarithmic lattices and singularities of Euler flow, Master's thesis, IMPA.

https://doi.org/10.1017/jfm.2025.10604 Published online by Cambridge University Press

CAMPOLINA, C.S. & MAILYBAEV, A.A. 2018 Chaotic blowup in the 3D incompressible Euler equations on a logarithmic lattice. *Phys. Rev. Lett.* **121**, 064501.
CAMPOLINA, C.S. & MAILYBAEV, A.A. 2021 Fluid dynamics on logarithmic lattices. *Nonlinearity* **34** (7), 4684.
CHAVANNE, X., CHILLÀ, F., CASTAING, B., HÉBRAL, B., CHABAUD, B. & CHAUSSY, J. 1997 Observation of the ultimate regime in Rayleigh–Bénard convection. *Phys. Rev. Lett.* **79**, 3648–3651.
CHEN, X. & SREENIVASAN, K.R. 2021 Reynolds number scaling of the peak turbulence intensity in wall flows. *J. Fluid Mech.* **908**, R3.
CORTET, P.-P., CHIFFAUDEL, A., DAVIAUD, F. & DUBRULLE, B. 2010 Experimental evidence of a phase transition in a closed turbulent flow. *Phys. Rev. Lett.* **105**, 214501.
CORTET, P.-P., DIRIBARNE, P., MONCHAUX, R., CHIFFAUDEL, A., DAVIAUD, F. & DUBRULLE, B. 2009 Normalized kinetic energy as a hydrodynamical global quantity for inhomogeneous anisotropic turbulence. *Phys. Fluids* **21** (2), 025104.
COSTA, G., BARRAL, A. & DUBRULLE, B. 2023 Reversible Navier–Stokes equation on logarithmic lattices. *Phys. Rev. E* **107**, 065106.
DEBUE, P. 2019 Experimental approach to the problem of the Navier–Stokes singularities. PhD thesis, Université Paris-Saclay, France.
DIRIBARNE, P. *et al.* 2021 Investigation of properties of superfluid ^{4}He turbulence using a hot-wire signal. *Phys. Rev. Fluids* **6**, 094601.
DOERING, C.R. & FOIAS, C. 2002 Energy dissipation in body-forced turbulence. *J. Fluid Mech.* **467**, 289–306.
DUBRULLE, B. 2024 Log at first sight. *J. Fluid Mech.* **1000**, F6.
DUBRULLE, B., DAUCHOT, O., DAVIAUD, F., LONGARETTI, P.-Y., RICHARD, D. & ZAHN, J.-P. 2005 Stability and turbulent transport in Taylor–Couette flow from analysis of experimental data. *Phys. Fluids* **17** (9), 095103.
EYINK, G.L. & PENG, L. 2024 Space-time statistical solutions of the incompressible Euler equations and Landau–Lifshitz fluctuating hydrodynamics. arXiv: 2409.13103.
GALLAVOTTI, G. 1996 Equivalence of dynamical ensembles and Navier–Stokes equations. *Phys. Lett. A* **223** (1), 91–95.
LATHROP, D.P., FINEBERG, J. & SWINNEY, H.L. 1992*a* Transition to shear-driven turbulence in Couette–Taylor flow. *Phys. Rev. A* **46**, 6390–6405.
LATHROP, D.P., FINEBERG, J. & SWINNEY, H.L. 1992*b* Turbulent flow between concentric rotating cylinders at large Reynolds number. *Phys. Rev. Lett.* **68**, 1515–1518.
LOHSE, D. 1994 Crossover from high to low Reynolds number turbulence. *Phys. Rev. Lett.* **73**, 3223–3226.
LOHSE, D. & SHISHKINA, O. 2024 Ultimate Rayleigh–Bénard turbulence. *Rev. Mod. Phys.* **96**, 035001.
MCKEON, B.J., LI, J., JIANG, W., MORRISON, J.F. & SMITS, A.J. 2004 Further observations on the mean velocity distribution in fully developed pipe flow. *J. Fluid Mech.* **501**, 135D147.
MÉTHIVIER, L., BRAUN, R., CHILLÀ, F. & SALORT, J. 2022 Turbulent transition in Rayleigh–Bénard convection with fluorocarbon(a). *Europhys. Lett.* **136** (1), 10003.
MONCHAUX, R. 2007 Approche statistique des écoulements turbulents. PhD thesis, Dynamique des fluides et des transferts Paris, France.
PAOLETTI, M.S., VAN GILS, D.P.M., DUBRULLE, B., SUN, C., LOHSE, D. & LATHROP, D.P. 2012 Angular momentum transport and turbulence in laboratory models of Keplerian flows. *Astron. Astrophys.* **547**, A64.
PIKEROEN, Q., BARRAL, A., COSTA, G., CAMPOLINA, C., MAILYBAEV, A. & DUBRULLE, B. 2024 Tracking complex singularities of fluids on log-lattices. *Nonlinearity* **37**, 115003.
PIROZZOLI, S. 2024 On the streamwise velocity variance in the near-wall region of turbulent flows. *J. Fluid Mech.* **989**, A5.
RAVELET, F. 2005 Bifurcations globales hydrodynamiques et magnétohydrodynamiques dans un écoulement de von Kármán turbulent. PhD thesis, Ecole polytechnique, France.
RAVELET, F., CHIFFAUDEL, A. & DAVIAUD, F. 2008 Supercritical transition to turbulence in an inertially driven von Kármán closed flow. *J. Fluid Mech.* **601**, 339–364.
ROCHE, P.-E. 2020 The ultimate state of convection: a unifying picture of very high Rayleigh numbers experiments. *New J. Phys.* **22** (7), 073056.
ROUSSET, B. *et al.* 2014 Superfluid high Reynolds von Kármán experiment. *Rev. Sci. Instrum.* **85** (10), 103908.
SAINT-MICHEL, B. *et al.* 2014 Probing quantum and classical turbulence analogy in von Kármán liquid helium, nitrogen, and water experiments. *Phys. Fluids* **26** (12), 125109.
SCHEEL, J.D. & SCHUMACHER, J. 2017 Predicting transition ranges to fully turbulent viscous boundary layers in low Prandtl number convection flows. *Phys. Rev. Fluids* **2**, 123501.

https://doi.org/10.1017/jfm.2025.10604 Published online by Cambridge University Press

SHRAIMAN, B.I. & SIGGIA, E.D. 1990 Heat transport in high-Rayleigh-number convection. *Phys. Rev. A* **42**, 3650–3653.

SHUKLA, V., DUBRULLE, B., NAZARENKO, S., KRSTULOVIC, G. & THALABARD, S. 2019 Phase transition in time-reversible Navier–Stokes equations. *Phys. Rev. E* **100** (4), 043104.

STEVENS, R.J.A.M., BLASS, A., ZHU, X., VERZICCO, R. & LOHSE, D. 2018 Turbulent thermal superstructures in Rayleigh–Bénard convection. *Phys. Rev. Fluids* **3**, 041501.

SWANSON, C.J., JULIAN, B., IHAS, G.G. & DONNELLY, R.J. 2002 Pipe flow measurements over a wide range of Reynolds numbers using liquid helium and various gases. *J. Fluid Mech.* **461**, 51–60.

VAN GILS, D.P.M., BRUGGERT, G.-W., LATHROP, D.P., SUN, C. & LOHSE, D. 2011 The Twente turbulent Taylor–Couette (T3C) facility: strongly turbulent (multiphase) flow between two independently rotating cylinders. *Rev. Sci. Instrum.* **82** (2), 025105.

https://doi.org/10.1017/jfm.2025.10604 Published online by Cambridge University Press